Physics – Uspekhi **63** (1) 67 – 82 (2020)

CONFERENCES AND SYMPOSIA

PACS number: **06.30.–k**

Diffraction limited X-ray optics: technology, metrology, applications

N I Chkhalo, I V Malyshev, A E Pestov, V N Polkovnikov, N N Salashchenko, M N Toropov

DOI: https://doi.org/10.3367/UFNe.2019.05.038601

Contents

Abstract. **Progress in the fabrication technology of normal incidence multilayer interference mirrors permits the traditional optical methods of microscopy, astronomy, and lithography to be transferred to the vacuum ultraviolet (VUV, wavelength: 10–200 nm) and the long-wavelength part of the soft X-ray (SXR, wavelength: 2–10 nm) ranges. Due to the short wavelength and properties of interaction with the substance, the radiation of these ranges provides unique opportunities in nanophysics, nanotechnology, and nanodiagnostics of matter. To use the potential of a short wavelength in full, diffraction-limited optical elements are required. Compared to traditional optical elements, their accuracy must be at least two orders of magnitude higher. The article provides an analysis of the real capabilities of traditional methods of making and studying precision optical elements and reports on the methods of fabrication and characterization of diffraction-limited optics for the VUV and SXR ranges developed at IPM RAS. Examples of the use of these optical elements for the tasks of extraterrestrial astronomy, X-ray microscopy, and lithography are given.**

Keywords: multilayer X-ray mirror, diffraction-quality optics, interferometry, aspherical surface, ion etching, roughness, X-ray microscopy, astronomy, lithography

1. Introduction

Interest in vacuum ultraviolet (VUV) (wavelengths of 10–200 nm) and soft X-ray (SXR) (wavelengths of 1–10 nm) radiation is caused by several factors. The short wavelength can, in principle, provide the nanometer spatial resolution required in microscopy and lithography [1, 2]. This spectral range includes atomic transitions, radiation of impurity ions in a high-temperature plasma, and the maximum of solar corona radiation [3]. This is used for rapid and precise chemical analysis of matter, including light elements, and for plasma diagnostics in thermonuclear studies. The imaging spectroscopy of the solar corona is the main method for fundamental physical studies of the Sun. In the VUV range, Earth looks 'black' from the space, and therefore atmospheric noise (excluding lightning) and solar light do not hamper the observation of even weak radiation in this spectral range from objects in near space. The latter property is used in hyperspectral instruments for remote probing of Earth and in systems for tracing of moving objects in near space [4–6]. This far from complete list demonstrates numerous applications of VUV and SXR radiations in diverse fields of science and technology.

However, a spatial resolution (δx) comparable to the wavelength (λ), $\delta x \approx \lambda$, could not be achieved in the X-ray range for a long time. This is related to the specific features of the interaction of X-rays with matter manifested in physical restrictions of the possibilities of optical elements. Because the refraction optics cannot be used in the spectral range of interest to us due to strong absorption, imaging can be performed only with the help of mirrors and diffraction optical elements (Fresnel zone plates).

The resolution of Fresnel optics is restricted by relatively small numerical apertures $\mathrm{NA} \leqslant 0.1$. Fresnel optics is characterized by low geometrical and angular apertures, low diffraction efficiency, and chromatic aberrations [7]. For this reason, applications of Fresnel optics are restricted in fact by microscopy [8–13].

Mirror X-ray optics, both grazing and normal incidence, has had much broader applications in astronomy and lithography. The operation angles of grazing-incidence mirrors are restricted by the total external reflection angle, and in the SXR range they lie, as a rule, in the region of $3-6^\circ$ [14]. The spatial resolution of such mirrors is restricted by the relatively low numerical aperture $\mathrm{NA} \sim 0.1$ and strong aberrations of mirrors for grazing incidence angles.

N I Chkhalo (*), **I V Malyshev, A E Pestov, V N Polkovnikov, N N Salashchenko, M N Toropov**
Institute for Physics of Microstructures, Russian Academy of Sciences, ul. Ul'yanova 46, 603950 Nizhny Novgorod, Russian Federation
E-mail: (*) chkhalo@ipm.sci-nnov.ru

Received 4 July 2019
Uspekhi Fizicheskikh Nauk **190** (1) 74 – 91 (2020)
Translated by M N Sapozhnikov; edited by V L Derbov

Normal-incidence multilayer interference mirrors can provide a fundamentally new possibility of achieving nanometer spatial resolution. Their use became possible due to recent progress in the technology of deposition of multilayer structures with a period equal to half the radiation wavelength. Reflection coefficients in the wavelength region of 2.4–30 nm being obtained at present by various groups lie in the range 10–72% [15–18], which can be used in various imaging schemes.

The main problem preventing the achievement of a resolution comparable to the radiation wavelength is the extremely rigid requirements on the quality of substrates for multilayer mirrors. Because the wavelengths of interest to us are 1–2 orders of magnitude smaller than in the optical range, the requirements on the roughness and accuracy of the shape increase correspondingly. While in optics values at the level of a few tens of nanometers are acceptable, in the SXR range, the acceptable level is 0.1–0.2 nm. As analysis has shown (see, e.g., [19, 20]), along with the 'ultraprecision' and 'ultrasmoothness' of substrates for mirrors, some additional requirements exist which complicate the fabrication of mirrors. In particular, the image quality depends on the roughness (irregularities, surface defects) in a broad range (nine orders of magnitude) of spatial frequencies (in the lateral scale, from 1 nm to the mirror size). Low-frequency roughness with lateral sizes of 1 mm–1 m, as a rule, cause distortion of the image as a whole. The resolving power most strongly depends on the middle frequencies (lateral sizes from 1 μm to 1 mm), because the waves scattered at these frequencies fall into the Bragg reflection peak of a multilayer mirror and, respectively, undergo interference amplification, as well as specular reflected waves. This leads to a strong blurring of the image edges. The waves scattered from a high-frequency roughness propagate outside the Bragg peak, their intensity is low (the integrated intensity does not exceed a few percent), and therefore they do not affect the resolution, but only reduce the image brightness. The specific feature of optics for the SXR and VUV regions is that the number of mirrors in a setup should be minimal, because reflection coefficients are often considerably lower than unity, while laboratory radiation sources are relatively weak. Therefore, to achieve a high resolution and large vision fields, aspherical mirrors should be used. Note that classical ellipsoids, paraboloids, and hyperboloids, i.e., second-order surfaces, are unsuitable in this case, and higher-order aspherics should be used [21–24].

Thus, the fabrication of the necessary optical elements required the revision of the possibilities of conventional methods of metrology and processing (polishing, aspherization) the surface of optical elements, as well as the adaptation of methods for solving these problems or the development of new methods satisfying requirements on diffraction-quality optics for the VUB and SXR ranges.

In this paper, we describe approaches developed in these three areas. We present the results of our studies and examples of applications of such optics for studying the solar corona, for remote probing near-Earth space, and in microscopy and lithography in the VUV and SXR ranges.

2. Methods for measuring shapes of mirror surfaces and aberrations of optical systems

Errors in the surface shape are conventionally called long-wavelength roughnesses with the lateral size ranging from the diameter of an object under study to 1 mm. The long-wavelength roughnesses of optical elements and aberrations of optical systems are traditionally measured with interferometers comparing wavefronts reflected from the object under study and a reference one [25]. The absolute measurement accuracy of commercial interferometers, despite the high relative measurement accuracy (up to $\lambda/1000-\lambda/3000$ for the root-mean-square deviation (RMSD) parameter [26]) rarely exceeds $\lambda/20-\lambda/50$. The reasons are the imperfection of commercial reference standards; their deformation during mounting into instruments and due to gravitation; the aging of metal holders followed by the redistribution of mechanical stresses; the propagation of the working (reflected from the object under study) and reference wavefronts through optical elements of the interferometer, where an uncontrollable phase incursion occurs; etc.

To achieve the required measurement accuracy, the 'ideal' interferometer should not use references and should provide 'self-calibration'. The idea of referenceless interferometry was put forward by V P Linnik back in the 1930s [27], who proposed using a spherical wave appearing upon diffraction of light from a small hole in an opaque screen (film) as the reference wave. The simplest calculations performed within the framework of the scalar diffraction theory for a superconducting material show that within diffraction peaks (in the case of $\lambda/d > 1$, where d is the hole diameter, one peak is observed, while for $\lambda/d \ll 1$, several peaks are observed) the phase front remains 'perfectly' spherical, despite the strong angular dependence of the radiation intensity. Interferometers of this type were called point diffraction interferometers (PDIs). The self-calibration of PDIs can be performed by the interference of coherent waves from two closely spaced holes [28].

Because PDIs are complicated in operation, we will additionally discuss this issue below. These interferometers gained acceptance only in the mid-1990s in connection with the problem of projection lithography at a wavelength of 13.5 nm. The subnanometer measurement accuracy of the PDI was first demonstrated in [29], where the reference spherical wave was produced by the diffraction of light at the output of a single-mode optical fiber with the polished end. However, because of the relatively large diameter of the fiber core $d \approx 4$ μm, the operating aperture of the interferometer proved to be extremely small, which greatly restricted the further development of PDIs of this type.

Instead, PDIs with a hole as the source of a spherical wave were developed [30–33]. This was facilitated by advances in microlithography making possible the fabrication of high-quality submicron holes. However, theoretical studies and practical applications of interferometers of this type revealed a number of physical and technological factors restricting the measurement accuracy and the field of applications.

Fundamental factors affecting aberrations of a wave diffracted from a hole in a metal screen include the interaction of secondary waves with the material of the hole, which are manifested, in particular, in the propagation of light through the edges of the hole within a skin-layer thickness, and excitation of plasmon–polaritons. The roughness of the edge of the hole and polarization effects also affect aberrations of the generated wavefront. These effects are described in more detail in [31, 34, 35].

The operation of PDIs is complicated by the high sensitivity (in fact, at a level of several hundred nanometers) of aberrations of the diffracted wave to the accuracy of combining the axes of a focused laser beam and the hole and

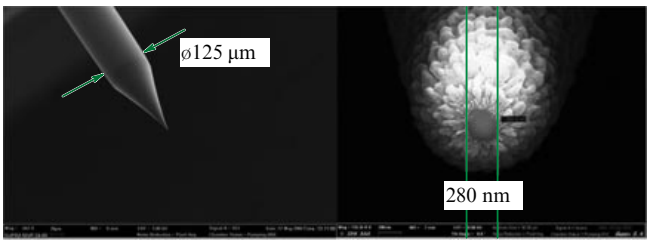

Figure 1. Electron microscope images of a source of the reference spherical wave based on a single-mode optical fiber with a subwavelength exit aperture.

to the aberrations of lenses focusing laser radiation on the hole [31, 36]. The problem is also complicated by the fact that these factors, especially the first one, are poorly controllable in practice. As a result, despite the high measurement accuracy, PDIs for industrial applications were not yet created for more than 20 years.

To minimize the problems considered above, we are developing diffraction reference wave interferometry based on a source of the reference spherical wave proposed in [37]. The source is based on a single-mode optical fiber with a cone metallized over the generatrix and a subwavelength exit aperture (Fig. 1). This approach [38] is based on the fact that, to perform precision measurements, even upon increasing the exit aperture, not only low aberrations but also the optimal wavefront intensity, when the output wave intensity is already sufficient for the reliable operation of a detector and only a single mode is emitted, are important. Aberrations of the diffracted wave and errors introduced by a detecting optical system are measured in a direct Young experiment, which allows us to assign this method to the class of so-called *ab initio* methods. At present, this source has record low wavefront aberration [39].

Because gravitational distortions of the shape are important at this accuracy level, optical elements should be tested in the operation position with respect to Earth's gravitational field. We developed a series of interferometers with different optical table lengths and different orientations of optical axes. Figure 2 shows photographs of three interferometers. The optical table length of the largest interferometer is 4.8 m. For systems with a large focus, it is necessary to use wavefront correctors or steering mirrors requiring special calibrations.

The main feature of interferometers is the broad use of fiber optic technologies. Beamsplitters, polarization controllers, delay lines, transmission channels, and phase modulators are fabricated using fiber optic technologies. In fact, an interferometer consists of one (or two, if necessary) source of a reference spherical wave and a video camera for recording interference patterns. A laser and other optical elements can be placed at a large enough distance and connected with spherical wave sources by optical fibers. This feature of the interferometer offers unique possibilities to researchers. The interferometric part can even be placed inside small-size instruments, in vacuum chambers, where optical aberrations should be directly controlled. Measurements can be performed in different climatic rooms, were the maximum temperature is limited only by the operation conditions of the video camera.

Applications of these interferometers for many years have demonstrated their high technical characteristics, reliability, and simplicity in operation, and the possibility of building

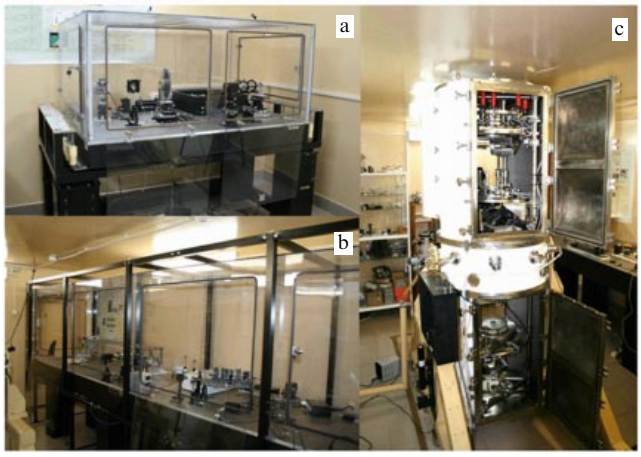

Figure 2. Photographs of (a) a horizontal interferometer with a 900×1450-mm optical table, (b) a horizontal interferometer with a 900×4800-mm optical table, (c) a vertical vacuum interferometer for measuring components up to 450 mm in diameter and the radius of curvature up to 1400 mm.

such instruments for industry. At present, we are completing the creation of the world's first industrial point diffraction interferometer free of external reference. The interferometer is quite compact ($600 \times 400 \times 300$ mm in size) and can operate at both orientations of the optical axis with respect to Earth's gravitational field.

3. Roughness measurement methods

As mentioned in Section 2, it is suitable to divide roughnesses by the degree of influence of their different lateral scales on the resolution of optical systems into two ranges: mid-frequency roughness with the lateral size of 1 μm–1 mm and high-frequency roughness with the lateral size of less than 1 μm. The mid-frequency roughness is traditionally measured with white light interferometers (WLIs) [20, 40]. The high-frequency roughness is measured with atomic force microscopes (AFMs) [41]. Despite broad applications of the WLI and AMF methods and good agreement between their results in the overlap of their operation ranges (see, e.g., [42, 43]), a strong discrepancy between the results of measurements by these methods was pointed out in some papers [44, 45]. The reasons can be quite different. For example, when silicon plates were etched by argon ions, micrometer and submicrometer pores appearing on their surface increased the surface roughness by an order of magnitude. However, this did not affect the roughness measurement results because of the limited lateral resolution of the WLI [46].

In addition, the results of WLI measurements are affected by the noise of a piezoceramic scanner and mechanical vibrations and, of course, by the quality of the reference, which also has its own roughness [47]. Obviously, the influence of systematic WLI errors on the results of roughness measurements increases with improving quality of the surfaces under study.

Figure 3 presents power spectral density (PSD) functions for the roughness of fused silica substrates with different effective roughnesses σ_{eff} obtained by integrating the PSD function: $\sigma_{\text{eff}} = 1.40$ nm (Fig. 3a), 0.33 nm (Fig. 3b), and 0.24 nm (Fig. 3c). Red curves correspond to the AFM, the 2×2-μm frame, circles to the AFM, the 40×40-μm frame, the thick black curve to the WLI, and the curve with squares

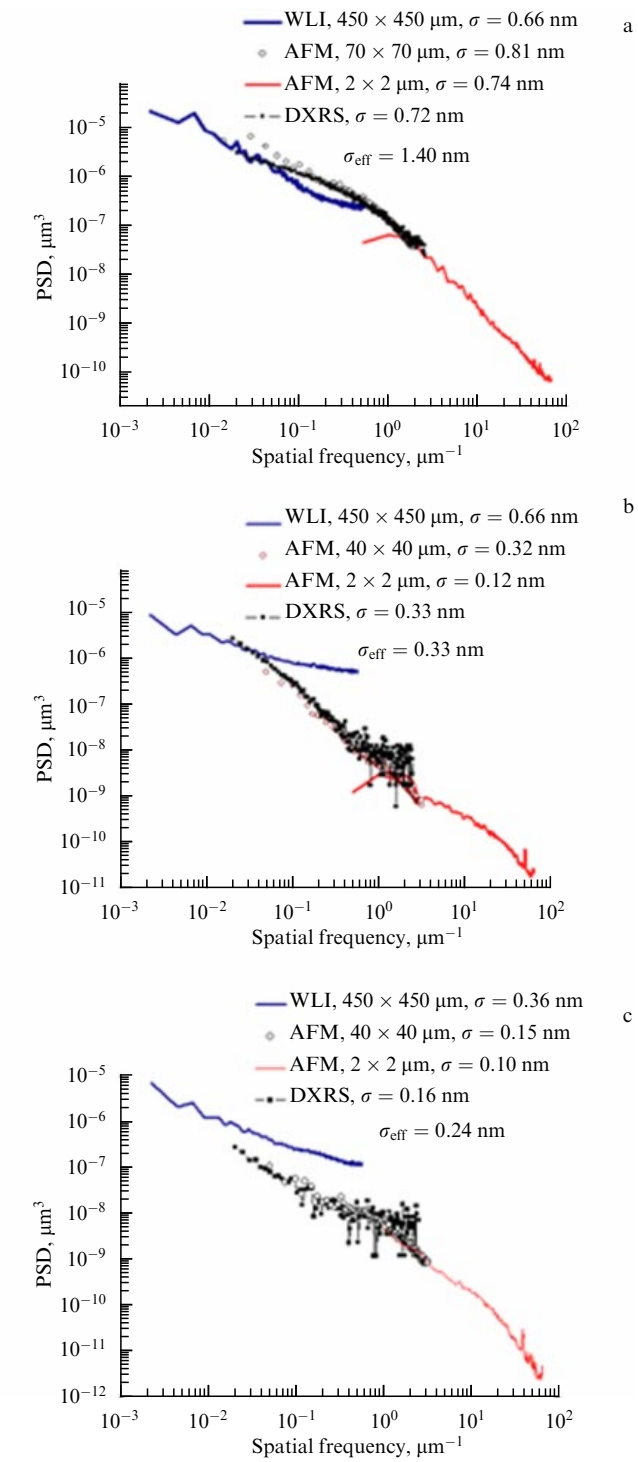

Figure 3. (Color online.) Power spectral densities (PSDs) of the roughness for silica plates with the effective roughness (a) $\sigma_{\text{eff}} = 1.40$ nm, (b) $\sigma_{\text{eff}} = 0.3$ nm, and (c) $\sigma_{\text{eff}} = 0.24$ nm.

to diffusion X-ray scattering (DXRS). One can see from the figure that, while for a substrate with $\sigma_{\text{eff}} = 1.40$ nm the results of measurements by these two methods in the overlap region of their operation ranges are in good agreement, the discrepancy becomes more and more noticeable with improvement in the polishing quality, up to the disappearance of crossings (Fig. 3c).

The WLI and AFM methods are not *ab initio* methods. In the WLI case, the reference surface is used, which introduces some uncertainty into the results of measurements. In the AFM, the measure of the distance from a probe (cantilever) to a surface is their interaction force, and therefore the results of measurements depend on a poorly controllable cantilever rigidness, which can lead to systematic errors in the roughness measurements. To minimize errors in the roughness measurements of supersmooth surfaces for X-ray applications, we completely excluded WLIs.

To measure the roughness in the spatial frequency range under study, we can use the DXRS as the ab initio method [48]. The theory of this method was developed in Refs [49, 50]. Important for practical applications of the DXRS method is the following. First, a direct relation exists between the angular intensity $I(\varphi)$ of diffusion X-ray scattering and the PSD(ν),

$$I(\varphi) = \frac{h\left|\pi(1-\varepsilon)t(\varphi_0)t(\varphi)\right|^2}{2l\lambda^3 \sin\varphi_0 \sqrt{\cos\varphi_0 \cos\varphi}}\,\text{PSD}(\nu)\,, \tag{1}$$

where h and l are the height and width of the detector slit, λ is the radiation wavelength, $t(\varphi)$ is the Fresnel radiation transmission coefficient, ε is the substrate material permittivity, and φ_0 and φ are the angles of incidence and scattering measured from the surface. For isotropic surfaces considered in most cases, the spatial frequency and angles are related by the expression

$$\nu = \frac{1}{\lambda}\,|\cos\varphi - \cos\varphi_0|\,. \tag{2}$$

The roughness is quantitatively described by the effective roughness in a certain range of spatial frequencies ν from $\nu_{\min}$ to $\nu_{\max}$,

$$\sigma_{\text{eff}}^2 = \int_{\nu_{\min}}^{\nu_{\max}} \text{PSD}(\nu)\,\mathrm{d}\nu\,. \tag{3}$$

Therefore, the results of roughness measurements are considered reliable only when the results of AFM and DXRS for flat test samples completely coincide (see Fig. 3). Some deviation of diffusion scattering curves in the right parts of Figs 3a, b is caused by detector noise.

Because expression (1) is valid only for small grazing incidence angles (the limitations of this method are described in more detail in papers mentioned above), the method can be used only for studying flat surfaces. The imaging optics, as a rule, are curvilinear, and for this reason the DXRS method is used in fact for AFM calibration (testing the operation correctness).

We developed a special stand for AFM measurements of high-aperture and curvilinear substrates. A special feature of the stand is that the local normal at each point of the surface under study is set along a probe axis, thereby providing the maximum range of spatial frequencies of the roughness in which measurements are performed [51]. By changing the stand configuration, we can study various optical elements and also normal and grazing incidence optics (Fig. 4).

The DXRS method has another limitation [52] which should be taken into account in studies. In the presence of a damaged surface layer (which appears upon mechanical grinding–polishing and ion bombardment), scattering from the volume inhomogeneities of this layer can even exceed scattering from the surface roughness, resulting in an erroneous interpretation of measurements. A simple method for detecting this layer is described in [46].

The problem with measuring mid-frequency roughnesses is limitations in the long-wavelength part of the spatial frequency spectrum of roughnesses. For the DXRS, these

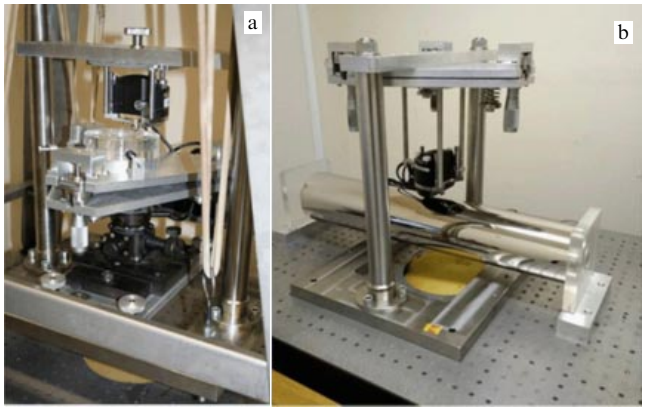

Figure 4. Photographs of a stand for AFM roughness measurements: (a) normal incidence and (b) grazing incidence substrates.

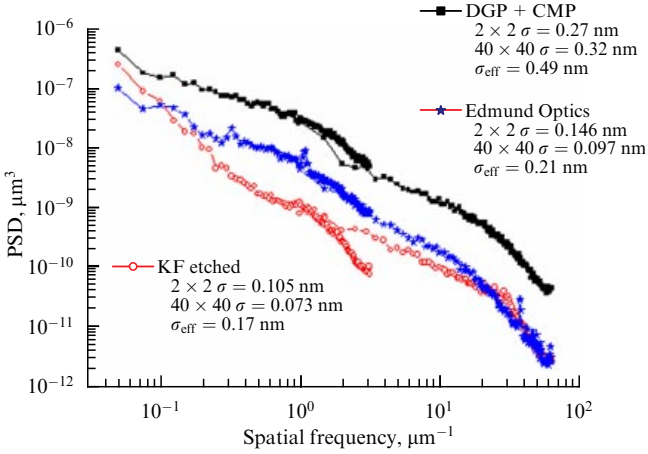

Figure 5. Roughness PSDs for fused silica substrates fabricated by different manufacturers: for substrate processed by the standard DGP + CMP method (squares), manufactured at Edmund Optics (asterisks), and manufactured by the improved DGP + CMP method with a final polishing by 600-eV Xe ions (circles).

limitations appear in the frequency region $\nu_{\min} \approx 0.02\ \mu\text{m}^{-1}$ and are related to the difficulty of separating the diffusion and specularly reflected components of X-rays near the mirror reflection peak ($\varphi_0 \approx \varphi$) (see relation (2)). In the AFM case, limitations are caused by piezoscanner nonlinearity near $\nu_{\min} \approx 0.05\,\mu\text{m}^{-1}$. To expand considerably the mid-frequency spectrum of roughnesses down to $\nu_{\min} \approx 0.001\ \mu\text{m}^{-1}$, use of point diffraction interferometry was proposed [53]. Because the surface profile in interferometry is often represented by the expansion in Zernike polynomials [54], in [55] the relation was obtained between the number of Zernike polynomials and the maximum spatial frequency that they describe on the surface.

Thus, we can summarize the results of this section as follows. To adequately characterize the roughness of X-ray optical elements, measurements should be performed in a broad range of spatial frequencies, and the numerical values of the roughness should be presented indicating the range of spatial frequencies in which these values were obtained. Otherwise, the roughness data offered by manufacturers and researchers often have no physical meaning, because variation in the integration range of the PSD function can change the value of the effective roughness in a broad range. The results of WLI and AFM measurements of supersmooth surfaces should be confirmed at least on test flat samples by measurements using ab initio methods such as DXRS and PDI. We recommend not using WLIs at all for measuring the roughness of supersmooth surfaces.

Thus, the results of measurements can be considered reliable only when all the methods give the same result in the overlap region of their operation ranges.

At the Institute of Physics of Microstructures (IPM), RAS, a facility of equipment and experimental methods is being developed for reliable roughness measurements in the spatial frequency range of $10^{-3}-10^{2}\ \mu\text{m}^{-1}$ with a subangstrom accuracy. A few hundred samples from various manufacturers in the world were investigated by these methods, and the results of these studies convincingly demonstrated the features of these measurements and confirmed the correctness of our recommendations presented above.

4. Fabrication and shaping of ultraprecise substrates

The existence of adequate methods for measuring the roughness and shape of supersmooth and ultraprecise substrates for X-ray mirrors permits the improvement of available methods and development of new methods for fabricating substrates. The first stage of substrate fabrication includes a deep grinding–polishing (DGP). For fused silica and optical ceramics with a low linear expansion coefficient (glass ceramics, ULE (Ultra-Low-Expansion), and Zerodur), the typical effective roughness in the frequency range of 0.025–60 μm^{-1} is $\sigma_{\text{eff}} = 1.1-1.4$ nm. The use of chemical–mechanical polishing (CMP) reduces the effective roughness to $\sigma_{\text{eff}} = 0.3-0.4$ nm. Note that these values are almost two times worse than the results of leading foreign manufactures (Edmund Optics, Zeiss, Thales).

Researchers at IPM, RAS and the Lebedev Physics Institute, RAS developed an improved DGP–CMP process which provided polished fused silica and ULE ceramics a roughness in the spatial frequency range of 0.025–60 μm^{-1} at the level $\sigma_{\text{eff}} = 0.2$ nm, which is not inferior to the world's best achievements. Moreover, the final polishing by 600-eV xenon ions provided a roughness $\sigma_{\text{eff}} = 0.14$ nm taking AFM noise into account.

Figure 5 presents the corresponding PSD roughness functions. Squares show the PSD function of a fused silica substrate processed by the standard DGP–CMP method, asterisks correspond to the PSD function for a fused silica substrate fabricated at Edmund Optics, and circles show the PSD function of a substrate processed by the improved DGP–CMP process and a final polishing by 600-eV Xe ions. After polishing by xenon ions, the effective roughness was 0.17 nm and 0.14 nm taking into account AFM noise. This polishing level is sufficient for fabricating diffraction quality substrates for the SXR range.

In using ion polishing, it is necessary to pay attention to the appearance of a broken surface layer 3–4 nm in thickness [46] caused by ion implantation and producing distortions of the near order of atoms of the substrate material.

A key problem at the moment is the relatively low quality of the shape of commercial substrates. Figure 6a shows interferograms and the reconstructed maps of deviations of the surface shape from a sphere for a silica substrate with NA = 0.3 fabricated at an optical plant. These data are typical for commercial samples. The bend of interference

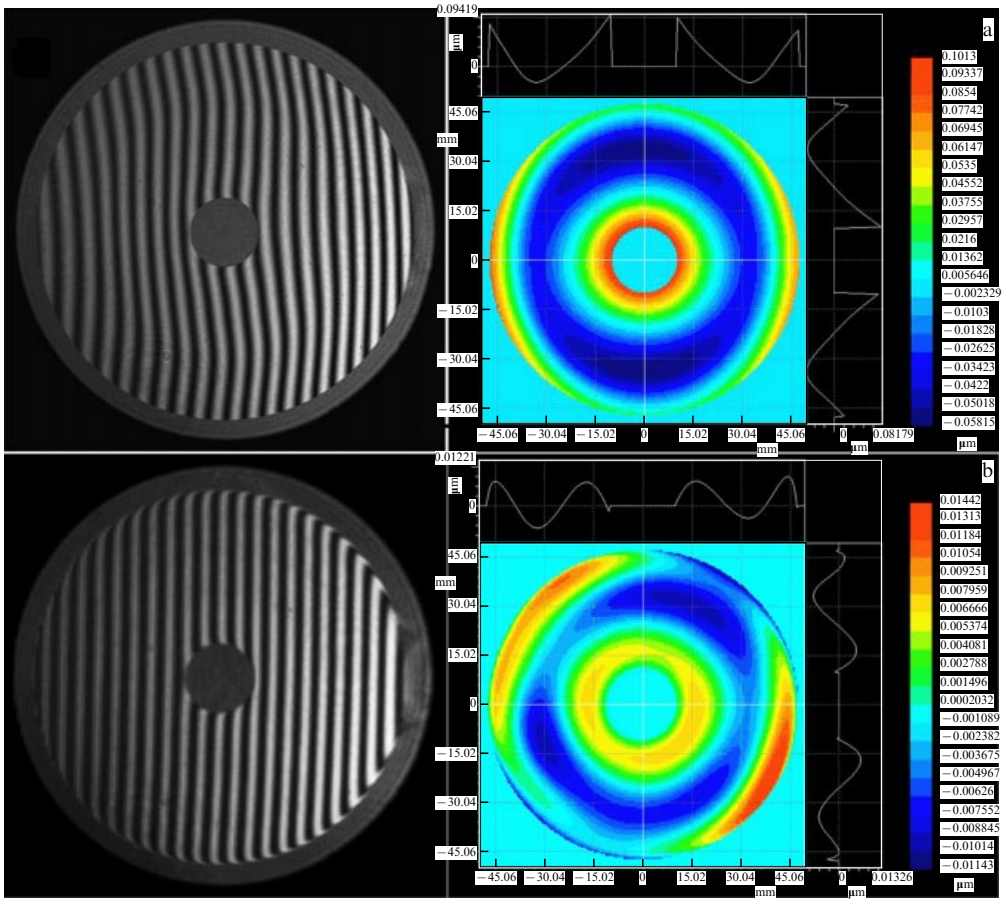

Figure 6. (Color online.) Interferograms and maps of the deviation in the surface shape from a sphere for a silicon substrate with the numerical aperture NA = 0.3: (a) substrate fabricated at an optical plant, (b) same substrate after mechanical grinding by the method developed at IPM, RAS.

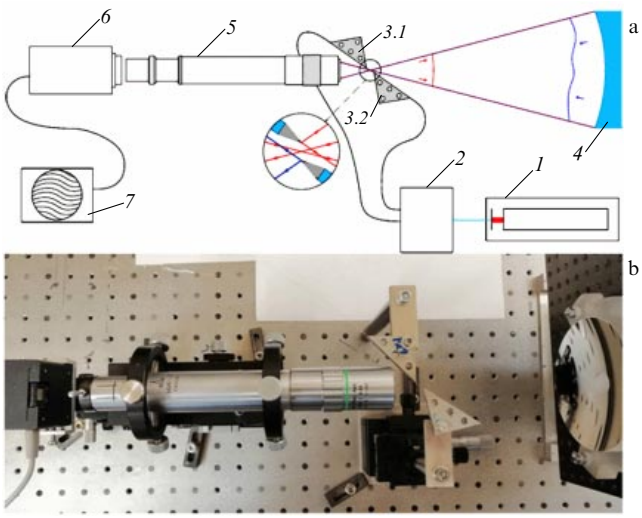

Figure 7. (a) Setup of a modified PDI imposing no restrictions on the reflection coefficient of a sample: *1* — He–Ne laser; *2* — controller for producing two coherent spherical waves and controlling the polarization, phase, and intensity of both waves; *3.1* and *3.2* — sources of reference spherical waves; *4* — surface under study; *5* — optical part of the detector system; *6* — digital video camera; *7* — computer. (b) Photograph of the modified PDI.

bands caused by surface aberrations is seen with the naked eye. The surface parameters are: the RMSD = 36 nm ($\approx \lambda/18$) and the range between the upper and lower points is 160 nm ($\approx \lambda/4$). These parameters are two orders of magnitude inferior to requirements on the diffraction quality optics in the X-ray range.

At IPM, RAS, an optical laboratory was created for the final refinement of the shape of substrates by mechanical grinding. The operative metrology of the surface shape was performed with a modified PDI not requiring the metallization of the component under study. A photograph and the setup of the interferometer are presented in Fig. 7. This setup does not use the plane mirror applied in traditional ones for studying spherical substrates with the help of PDIs [31, 39] for redirecting the reflected operation wavefront carrying information on the surface shape to a detector. In this PDI setup, the reference spherical wave from one source is directed onto the component under study (*3.1* in Fig. 7), while the second source (*3.2*), coherent with the first one and turned through 180° in the direction of the detector system, forms the reference wavefront. Because the maximum contrast of the interference pattern is achieved for equal intensities of the operation and reference fronts, a component under study in traditional PDIs should be covered with a reflection coating. This highly complicates and elongates the measurement procedure (to 1–2 days), whereas upon the final smoothing of the component surface, the polishing duration up to the next measurement of the surface shape can be less than half an hour. In the proposed DPWI scheme, the intensity, polarization, and phase shift of two coherent waves are controlled with the help of specially developed controller *2*.

Figure 6b shows the interferogram and the surface map of the same substrate after finishing the surface shape that we

performed by grinding for one week. One can see that our method for finishing optical surfaces provided an improvement in the component precision only for two weeks of processing by a factor of 6.8 in the RMSD parameter, RMSD = 5.3 nm ($\approx \lambda/120$), and the maximum difference in the profile heights by a factor of 6.1, down to 26 nm ($\approx \lambda/24$). This result was achieved by processing the unloaded component. The component grinding process was corrected by performing precision PDI measurements of the component shape through short time intervals (less than 1 h) with a time lag sufficient for the complete thermalization of the component.

Due to controllability of the technological process, ion-beam etching is more and more often used for the final processing of precision optical parts. It was first used for aspherization of initially spherical substrates for astronomical mirrors [56, 57]. Due to increased requirements on the roughness of substrates, many papers appeared devoted to the study of the influence of ion-beam etching parameters on the morphology and roughness of surfaces of various optical materials [58–66]. Fused silica of different types, optical ceramics (glass ceramics, ULE, and Zerodur), and substrates made of crystal materials and metals were investigated. Based on these studies, the following practically important conclusions can be made. First, the smoothing of the high-frequency roughness with lateral sizes of 1–2 μm and smaller is observed for substrates made of fused silica, optical ceramics, and some crystals. The optimal energy of ions depends on the material and kind of ions and lies in the range from 400 to 1000 eV. The optimal angles of incidence of an ion beam for polishing amorphous materials lie in the range of $0-40°$ from the normal, while the optimal angle for crystal materials can be substantially different [67–69]. Second, the ion polishing of metal substrates, except using special technologies (see, e.g., [70–72]), as a rule, causes a strong degradation of the surface shape [73].

Another problem, which is solved using small-diameter ion beams, is the correction of local errors of the surface shape. This technology is required for manufacturing substrates with a subnanometer RMSD. At present, both specialized and commercial setups are being developed for these purposes [74–77]. Depending on the ion source type chosen, the setups can be used either only for aspherization and ion polishing [74, 75] or for correction of local errors [76, 77].

At IPM, RAS, a universal setup was developed to solve all these problems. Figure 8 shows external and internal views of this setup. Component *1* for processing is mounted on a five-coordinate scanning platform *2*. The ion polishing and aspherization of substrates is performed using a wide-aperture high-frequency source *3* or incandescent-cathode source *4* (most often used with hydrogen beams [70]). Local errors are corrected with the help of a small ion source *5*. The setup and influence of the ion beam size on the roughness frequency spectrum, which can be removed by this method, are described in more detail in [78].

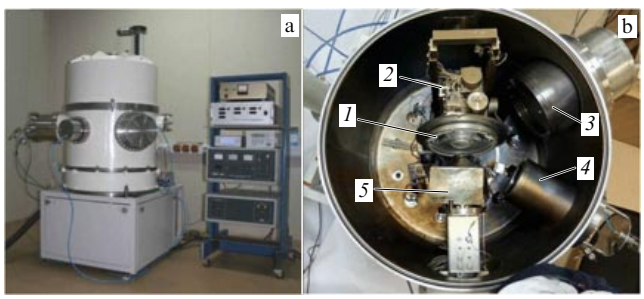

Figure 8. Photographs of the setup for the ion-beam processing of optical components (a) outside and (b) inside. *1* — processed component, *2* — five-coordinate scanning platform, *3* — wide-aperture HF ion source, *4* — incandescent cathode source, *5* — small ion source.

5. Applications of developed optical devices in science and technology

Methods for the metrology and fabrication of precise optical elements developed by the authors of this paper allowed the development of instruments with unique characteristics for various scientific and technological applications. In this paper, we consider four applications: the study of the solar corona, the VUV range monitoring of near space, SXR microscopy, and X-ray lithography.

5.1 Optical elements for solar corona studies

Historically, the first applications of imaging optics were cosmic missions for studying the solar corona in the VUV range developed at the Lebedev Institute, RAS. Multilayer mirrors and absorption filters were developed and fabricated at IPM, RAS. Participation in these studies began in 1988 with the Fobos station [79], then KORONAS-I [80], KORONAS-F, and the last KORONAS-Foton [82] project (KORONAS is the abbreviation of Complex Orbital Near-Earth Observation of Solar Activity (in Russian)). Telescopes were built using the Ritchey–Chrétien scheme. The aspherization of the surface of substrates was performed by the deposition of multilayer mirrors with the period gradient along the surface [83]. Figure 9 illustrates the dynamics of the resolving power of optics fabricated by us from mission to mission. It can be seen that the resolution improved with each subsequent mission, and the Tesis telescope already had the nearly record resolution of 1.7 seconds of arc.

At present, we are involved in several solar projects being developed at the Lebedev Institute. The most complicated and interesting from the point of view of manufacturing optics is the Arka project [84]. A primary aspheric telescope mirror 250 mm in diameter will provide the record-high angular resolution (≈ 0.1 seconds of arc) for resolving structures down to 70 km in size on the Sun. To achieve the required resolution, the admissible error in the shape over the RMSD parameter should not exceed 1–2 nm. Aside from the difficulty of fabricating such a mirror, a number of problems appear which must be solved during its development. First, the mirror should be put in a metal mount without deforming its surface. Second, the mount with the mirror should be installed into a telescope, also without deformations. Third, during the launching of the spacecraft, fixture systems should withstand huge overloads, up to 1000 *g* without any plastic deformations in the system of fixing the mirror in the mount. Fourth, during imaging, the mirror temperature can vary in a broad range, up to $\pm 25°$, and image quality must not be impaired. And finally, the most difficult challenge is the necessity of taking into account the mirror deformation caused by gravitation on Earth, which disappears in the space flight.

Figure 10a shows a photograph of a primary mirror in a mount for the Arka telescope. The mirror in the mount is suspended on six plates over a circle under the interferometric

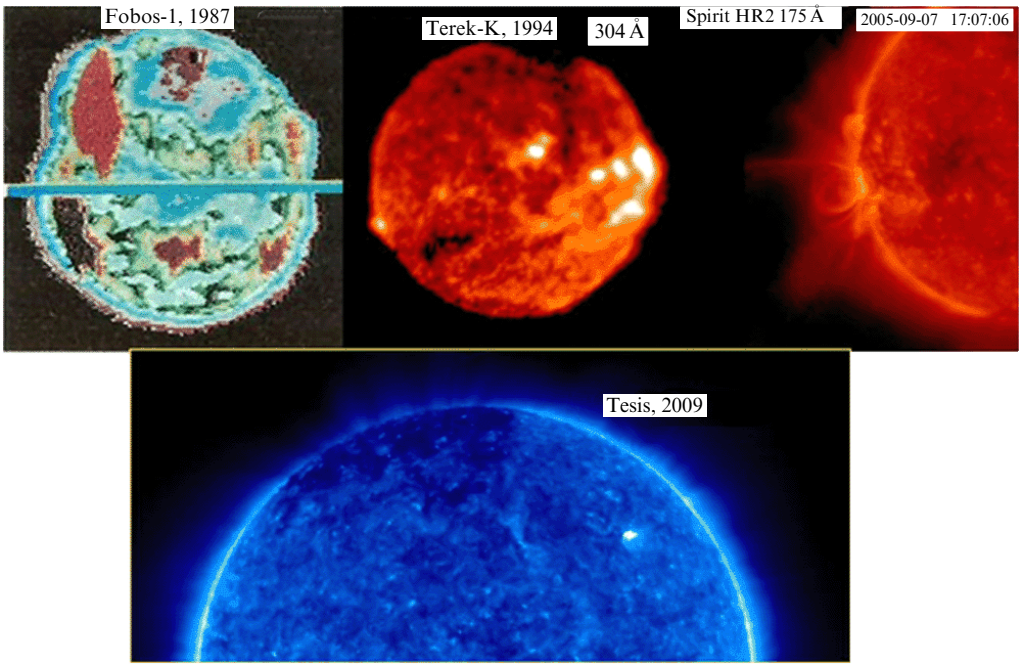

Figure 9. (Color online.) Solar corona images obtained in different years in the VUV range illustrating the resolution improvement from mission to mission.

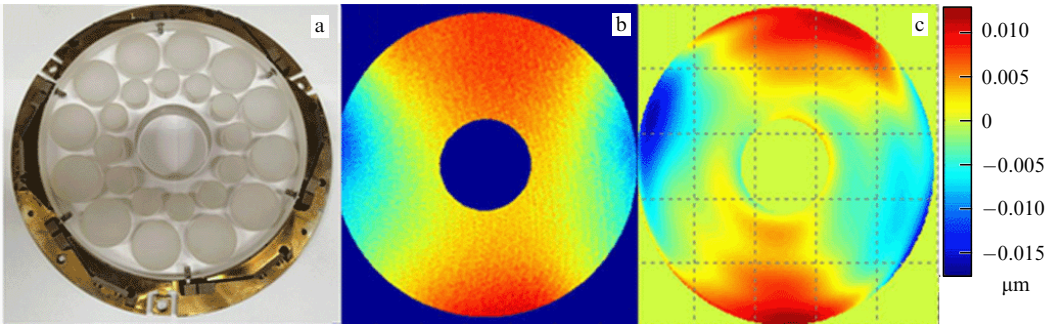

Figure 10. (Color online.) (a) Photographs of the model of a primary mirror for the Arka telescope in a holder. (b) Calculated map of the surface deformation caused by the component weight. (c) Measured map of the 'weight' deformation for the model of a primary mirror.

all-operation control block. The control guarantees minimal deformations of the surface shape during assembly. To minimize thermoinduced deformations produced by the linear expansion of materials, the mount and all fixture elements are made of a special titan-niobium TV-36 alloy with a thermal linear expansion coefficient of about 5×10^{-7}, as for fused silica.

During the fabrication of the mirror, its shape is controlled with the horizontal direction of the optical axis. Figure 10b shows the calculated map of the surface deformation caused by the component weight. The deformation has an astigmatic form with the RMSD = 4.0 nm and the maximum height difference (MHD) of 21 nm, which exceeds by almost four times the admissible error of the mirror shape. In this project, we plan to exclude this deformation by creating a mirror surface profile with the opposite sign. Correspondingly, in the case of zero gravity, the gravitational load will disappear and the mirror will 'straighten out'. The realization of this idea is illustrated in Fig. 10c showing the measured deformation map of the weight of the primary mirror model. The deformation parameters are: the RMSD = 4.5 nm and the MHD = 25 nm. This deformation is separated from the total error of the component shape by the rotation method described in [22]. The measured values slightly differ from the calculated ones, which is related to a rather large error in measuring the model mirror surface. The accuracy of these measurements can be improved. Thus, the methods developed for assembling the primary mirror into a mount and measuring gravitational distortions demonstrate the possibility of realizing the Arka project with specified characteristics. A detailed description of all the aspects of the mirror fixture in the mount and assembling in the telescope can be found in [85].

5.2 Modified Schmidt–Cassegrain scheme of an all-reflecting UV and VUV telescope

In the last decade, the expanding applications of space technologies have resulted in the development of new-generation systems for remote sensing of Earth (RSE) and near-Earth space [4–6]. Such systems are used to solve a variety of problems for studying natural resources, in agriculture, in cartography, in environmental monitoring, for special control of Earth's surface, etc.

Until recently, spectral images were mainly recorded in the visible and IR wavelength ranges. However, due to the expanding scope of problems, the interest of developers has extended to the UV range and even the VUV range, in which Earth is virtually 'black'. This permits the observation of rapidly flying objects even in daytime, both by the scattering of solar radiation at the 121.6-nm $H_{Ly\alpha}$ line and by molecular lines of atmospheric gases excited by moving hypersonic objects [5]. These ranges, especially the VUV range, are characterized by the following features. First, the absorption and strong dispersion of optical constants of materials resulting in chromatic aberrations restrict the choice of the basic optical scheme of a telescope to mirror systems (reflectors). Second, because radiation intensities are extremely low, wide-aperture optical elements are required, and the number of mirrors in the setup should be minimal to minimize losses.

Modern RSE systems use several reflector schemes. One of them is the Cassegrain system, consisting of a primary concave parabolic mirror and a secondary convex hyperbolic mirror. The field of view covers a few minutes of arc at a relative aperture of 1:3–1:5 [86]. The most popular is the modification of the Cassegrain system, the Ritchey–Chrétien system, in which the primary and secondary mirrors are hyperbolic. The field of view of the Ritchey–Chrétien system can be increased to 1° with the angular resolution of 2″ [87]. Such systems are convenient for use in long-focus instruments (the objective length can be a few times smaller than the focal distance), which makes them one of the most popular solutions for astronomical instruments such as the Hubble telescope [88]. These systems are rarely used in wide-aperture objectives because of the difficulty of fabrication and alignment and an increase in central screening. In practice, the Ritchey–Chrétien systems with a relative aperture of more than 1:4 are rarely used.

A system consisting of four spherical mirrors (two objective mirrors and two aberration correctors) eliminates the field aberrations of the system to a considerable extent and provides an angular field of view of up to 3° [89]. Significant disadvantages are the presence of three large (and therefore massive) mirrors that are complicated to fabricate and difficult to align, signal losses on additional mirrors, and considerable (up to 25% in the area) central screening. The low technological effectiveness of this system significantly impedes its application in VUV and UV instruments in space.

In on-board instruments in the visible spectral range, an off-axis mirror system, called in the literature the mirror Cooke triplet, has found applications and was mounted, for example, on the Topsat (Great Britain) [90] and EO-1 (USA) [91] satellites. The attractive feature of the mirror Cooke triplet is the field of view enlarged to $12-14°$ in the sagittal direction, which provides coverage of a large region without additional scanning. In this case, the field of view in the meridional direction is $1-2°$. For large relative apertures, residual aberrations essentially increase. The system also has a large size: the total area of the second, third, and fourth mirrors is approximately three times larger than the entrance pupil area.

A partially off-axis three-mirror system representing a modified Cassegrain system supplemented with a ternary mirror — a corrector of field aberrations — and a plane mirror is called a Korsch system. The system has an intermediate image and a real exit pupil [92]. The main image can be used only partially (the central part is excluded) because of the overlap with the intermediate image. Nevertheless, the effective field of view can be increased to $3-4°$. The maximum relative aperture is 1:3.5. The disadvantages are the large size along the optical axis and the restriction of the relative aperture, complicated aspherical mirror surfaces, strict requirements on the alignment accuracy, and the impossibility of observations at the center of the field of view. Nevertheless, the Korsch scheme is widely used in RSE systems, for example, in the Pleiades and Kompsat 3 telescopes [93].

Our analysis of optical systems with second-order aspherical mirrors showed that the four-mirror Korsch objective and the mirror Cooke triplet are the most convenient for use in high-resolution VUV and UV instruments with a field of view exceeding 1°. However, these systems are extremely complex, because they require the fabrication of large aspherical mirrors and precise alignment. Therefore, the problem of searching for new telescope systems surpassing the known ones in field of view and resolution and having the minimal number of surfaces remains urgent.

This problem has been at issue for many decades. Thus, Baker [94] proposed to supplement the Schmidt camera [95] with a secondary convex mirror. This scheme was called the Schmidt–Cassegrain telescope. The field of view of the system increased to 3° due to an aberration corrector in the form of a plane mirror with the axially symmetric fourth-order aspherical profile, while the shape of mirrors in the Cassegrain objective simplified to spherical. However, such a scheme with a reflection corrector was not realized for a long time because of the difficulty of a no longer axially symmetric aspherical corrector profile.

Due to the recent development of ion-beam methods for precise processing of optical elements, in particular, the possibility of fabricating higher-order aspherical surfaces, it became possible to realize the required setups. The one with a reflection aberration corrector, which was called the 'modified Schmidt–Cassegrain scheme' was first developed and realized in [96]. The optical setup of the telescope is presented in Fig. 11 and its main parameters are listed in Table 1. One can see that the telescope provides a subsecond resolution with a field of view of $\pm 1.5°$, which is 3–4 times bigger than the field of view of the Ritchey–Chrétien scheme. Along with technical characteristics, the proposed telescope scheme has a number of advantages making it very promising for hyperspectral instruments due to its low cost, technological effectiveness, and simple alignment due to the use of spherical mirrors in the objective. The allowance for the decentering of mirrors and the corrector is a few tenths of a millimeter, which can easily be achieved in practice. The main difficulty for traditional methods of mechanical shaping of optical elements is the fabrication of a planoid with the asphericity profile described by sixth-order Zernike polynomials and containing both axially symmetric and nonsymmetric components with a maximal aspherization depth of about 5 μm. However, with the use of ion-beam processing methods, this problem becomes routine.

Based on the considered scheme, the experimental prototype of a two-channel telescope for the UV and VUV ranges was constructed and, to determine the angular resolution of the telescope over the entire field of view, a wide-angle collimator was developed based on the 'Schmidt camera' with a planoid mirror for aberration corrections. The collimator has a subsecond resolution in the field of view of 3°. The field curvature was corrected with the help of a convex spherical

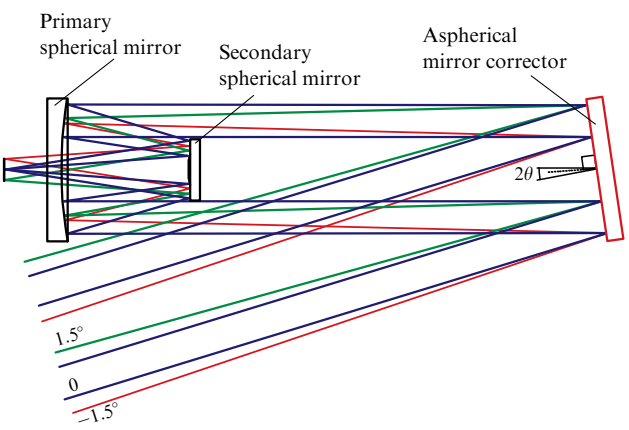

Figure 11. (Color online.) Optical scheme of a telescope based on the modified Schmidt–Cassegrain scheme. Beams entering the telescope at angles of 1.5°, 0, and −1.5° are shown by different colors. The main parameters of the telescope are presented in Table 1.

Table 1. Calculated telescope parameters.

Parameter	Value
Entrance pupil diameter D, mm	180
Effective focal distance F, mm	584.156
Relative aperture D/F	1:3.25
Image diameter, mm	30.4
Angular field of view 2ω, deg	3.0
Angular resolution in the field of view, sec. of arc	$\leqslant 1$
Field curvature in the image plane	Plane field
Distance between a planoid and the primary mirror, mm	747.00
Distance between mirrors, mm	178.425
Distance between the secondary mirror and the image plane, mm	258.425
Diameter/primary mirror curvature radius ratio	190/645.20
Diameter/secondary mirror curvature radius ratio	86/644.40

mire (a plate with a special pattern deposited on it). The collimator and the method of telescope attestation are described in detail in [97].

Figure 12 presents photographs of the optical part of a two-channel telescope connected with a collimator. Figure 12b shows mire images at different field points recorded in the telescope image plane, which showed that the resolution in the field of view proved to be better than 1.3 seconds of arc, which is close to the theoretical limit of 1″.

Thus, it is shown that ion-beam methods for shaping optical elements allow us to fabricate precise aspherical mirrors with unique characteristics, thereby improving the traditional schemes of telescopes and collimators and creating new ones that could not be realized earlier.

In concluding this section, we consider the outlook for using beryllium for space systems. Due to its low density and high rigidity, beryllium has already been in use for a few dozen years for fabricating construction materials and mirrors for space instruments [99–102]. Of the recent developments, the James Webb Space Telescope with the primary mirror 6.5 m in diameter should be distinguished, which should replace the world renowned Hubble Space Telescope [103]. The polishing and ion-beam processing of pure beryllium cannot provide supersmooth surfaces because of its polycrystalline structure [73]. This imposes fundamental restrictions on the possibility

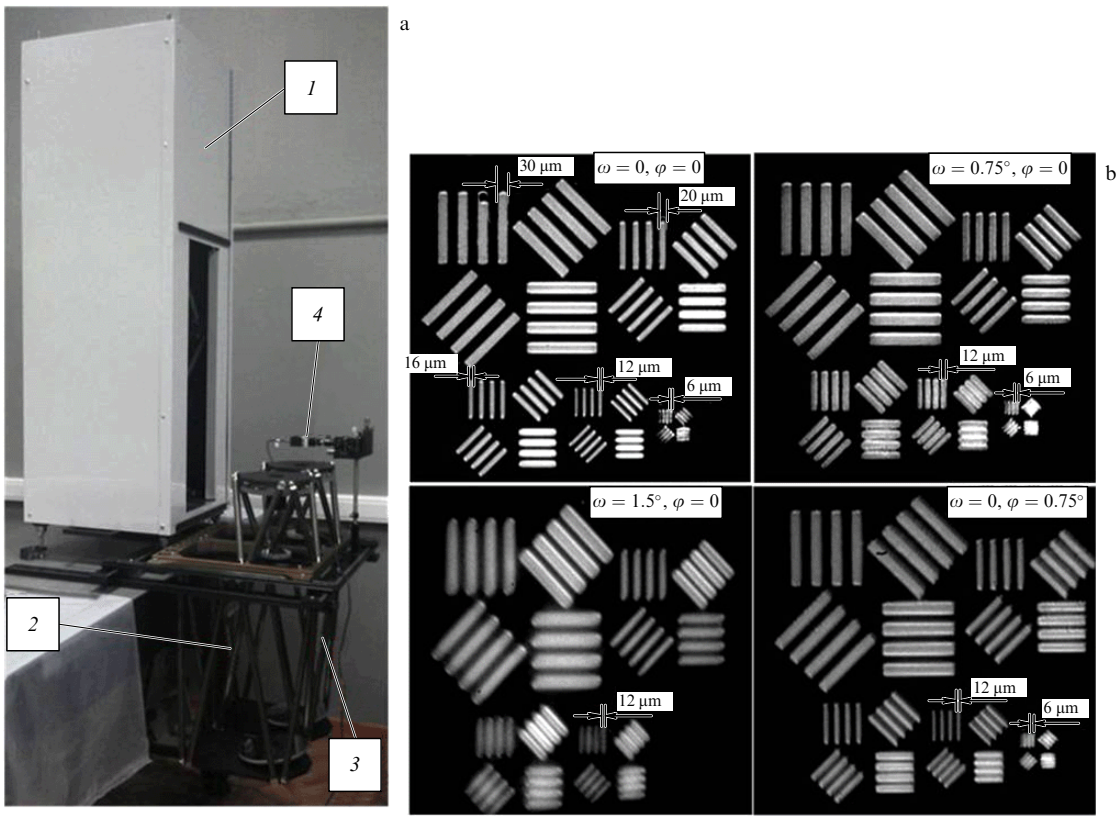

Figure 12. (a) Photograph of the optical part of a two-channel telescope with a collimator: *1* — collimator, *2* — 1st channel at wavelengths of 120–190 nm, *3* — 2nd channel at wavelengths of 200–380 nm, *4* — CCD camera. (b) Mire images at different field points recorded in the telescope image plane.

of precise aspherization and correction of local errors in the shape.

In practice, to improve the polishing quality, beryllium is covered with electrolytic nickel containing a large amount (about 10%) of phosphorus, thereby forming a quasi-amorphous layer on the surface. However, this is not sufficient for obtaining the roughness required for short-wavelength radiation. In [72], the possibility of ion-beam processing of beryllium substrates with a nickel coating was studied. It was found that at least the ion polishing of the nickel coating does not develop a surface roughness and allows one to perform the ion-beam precise aspherization and correction of local errors on such substrates. The ion polishing results [71, 72] suggest that beryllium mirrors with improved characteristics operating in the short-wavelength range for space applications will appear in the nearest future.

5.3 Soft X-ray microscopy

To understand the operation mechanisms of organic cells in modern biological problems and to study the influence of various diseases on them, it is necessary to see the details of living cells with a resolution of a few tens of nanometers [104–107]. Traditional diffraction-limited microscopy in the visible region cannot be applied for studying structures with parts smaller than 200 nm in the lateral direction and smaller than 700 nm in the axial direction [108]. Scanning electron microscopy (SEM) allows one to see the details of cells with a resolution of 0.3–5 nm [108, 109]. However, because of the strong scattering of electrons and a decrease in the signal with increasing sample thickness, it is necessary to cut samples into thin sectional layers (< 300 nm), which leads to the damage of tissues in cuts and prevents the well-defined combining of section images and the reliable reconstruction of a three-dimensional structure [110]. High exposure doses in SEMs cause the decomposition of organic samples under the action of the electron beam. In recent years, papers have been published on the angular 3D SEM tomography of cells without cutting samples. However, this approach can give the 3D structure only for the surface of samples [110, 111]. The atomic force and scanning tunneling microscopy provide nanometer resolution, but can be used only for surface studies [112].

Over the last 30 years, soft X-ray microscopy (SXRM) has been developed in the 'water transparency window' in the 2.3–4.4-nm wavelength range. Soft X-ray microscopy is characterized by the almost complete absence of scattering (five orders of magnitude weaker than absorption [1]), the resonance absorption of this radiation by carbon-containing proteins, fats, and carbohydrates, and good transmission in water (up to 10 μm). The advantage of SXRM over other spectroscopic methods is that the tomography of 'thick' (10–15 μm) samples can be performed with a nanometer resolution without cutting them into thin layers and using exposure doses much smaller than for SEM.

As an imaging element, Fresnel zone plates (FZPs) are traditionally used, which provide a lateral resolution of several tens of nanometers [10, 11, 107, 113, 114]. The use of a unique FZP with an extreme zone 12 nm in width and partially coherent illumination provided a resolution of about 10 nm for the image of a section of a multilayer film structure [115].

Tomography methods with the use of FZPs gave 3D images of objects with a resolution of 70–100 nm at the 20–40-nm diffraction limit of FZPs [12, 105, 106, 116]. A resolution of 70 nm was obtained by using highly monochromatic synchrotron radiation for cryogenically fixed samples [104, 106, 116].

Because of the high reflection coefficients and operation angular apertures of FZPs providing diffraction-limited resolution at the nanometer level and an intense probe signal, of special interest is the SXRM scheme based on a wide-aperture mirror Schwarzschild objective (SO). For example, for the typical numerical aperture NA = 0.3 and a wavelength of 3.37 nm, the diffraction limit, according to the Rayleigh criterion, is $\delta x = 0.61\lambda/\mathrm{NA} = 7$ nm and the depth of focus (DOF) $= \lambda/\mathrm{NA}^2 = 37.5$ nm, which allows one to carry out z-tomography with a nanometer resolution for reconstructing the 3D structure of samples. This requires the development of algorithms for the z-tomography taking into account strong absorption during the propagation of probe radiation through the sample and conical, rather than quasi-parallel, illumination of each point of the sample, as in the case of low-aperture objectives. In the literature, until recently, mirror SXR low-resolution or contact microscopes were mainly considered [117–121]. The development of high-resolution SXR microscopes based on the SO in the spectral region of the 'water transparency window' was hampered by the absence of commercial supersmooth substrates with a shape accuracy at the level of 0.1–0.2 nm for fabrication of multilayer optical elements.

Based on the new methods for fabricating high-precision optical elements, researchers at IPM, RAS are developing a microscope using a wide-aperture SO and z-tomography to obtain 3D structures of samples with a resolution better than 50 nm and decreasing the exposure time of each frame from several minutes to several seconds. The X-ray optical scheme of the microscope is shown in Fig. 13 [122]. X-rays were

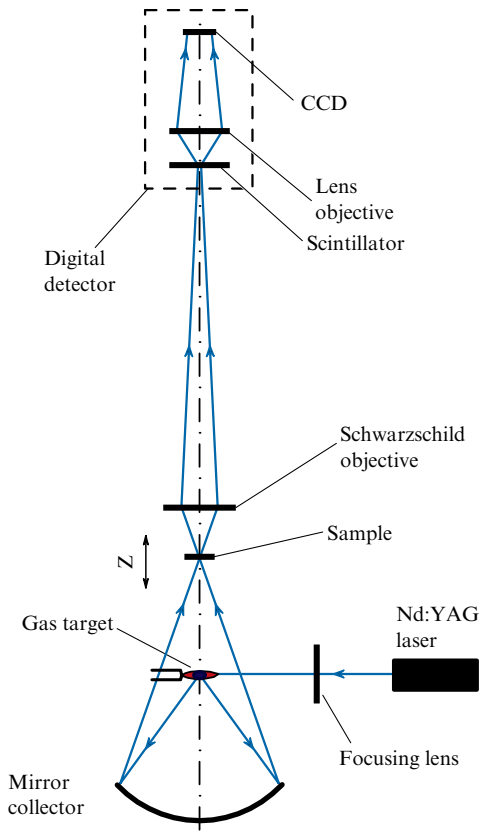

Figure 13. X-ray optical scheme of an SXRM with an SO.

obtained from a plasma produced upon interaction of a tightly focused 1.06-μm, 1-J, 4-ns pulse from an Nd:YAG laser (with a pulse repetition rate of 10 Hz) with a pulsed gas jet. The gas contained carbon. The operation line was the 3.37-nm, C(VI) 1s–2p spectral line of fivefold ionized carbon. The collector and objective mirrors had Cr/Sc coatings [123] with a reflection coefficient at this wavelength of more than 10%.

The X-ray optical system has two magnification levels. At the first level, the X-ray image of a sample is transferred with a 46× magnification on the entrance plane of a scintillator (YAG doped with Ce ions). Soft X-rays are transformed in the scintillator to visible radiation, which is collected by an optical system on a CCD video-camera. The scintillator surface and detector are located in the object and image planes, respectively. Due to the strong absorption of SXRs in the scintillator (the penetration depth is smaller than 1μm), the resolution is not impaired. The detector was tested in [124] and its resolution was 0.67 μm, which corresponds to the calculated resolution on the sample of about 14 nm.

The two-stage magnification system chosen here significantly simplifies the construction and alignment of the system and reduces the number of mirrors in the objective, reducing it to the well-known two-mirror Schwarzschild setup. In addition, to study a sample in detail in practice, it is necessary to investigate different scales of its components. In optical microscopy, this is performed with the help of objectives with various magnifications, which the two-stage magnification system permits. The X-ray objective has a fixed magnification, and the optical scheme of the detecting system allows one to change objectives. In this case, only a slight alignment of the CCD camera along the optical axis of the system is required. The detector uses long-focus 1.96×, 4.23×, and 20× Mitutoyo Plan Apo objectives.

The field of view of the microscope is determined by the CCD array size of 6.7×8.8 mm divided by the total magnification of the microscope (90×, 195×, 920×) and is from 7.3×9.5 to 74.5×97.5 μm^2. Table 2 presents the measured characteristics of the microscope.

Table 2. Microscope parameters for three objectives.*

Objective numerical aperture NA	0.14	0.28	0.55
Magnification of the detector optical system (×)	1.96	4.23	20
Spatial resolution of the detector, μm	3.3	1.0	0.65
SO magnification (×)	46		
Microscope magnification (×)	90	195	920
Field of view on a sample, μm^2	74.5×97.5	34.5×45.1	7.3×9.5
Microscope spatial resolution, nm	71	22	14

* All the parameter values, except the microscope spatial resolution, are experimental.

Tomography will be performed by moving a sample along the vertical (z-axis) with the help of piezoceramics. In this case, it is advantageous to have a projection objective with a large numerical aperture, because the DOF and spread along the optical axis are proportional to NA^{-2}. This approach to z-tomography operates well in the case of NA $\gg 0.1$ because of a small DOF. On the other hand, as follows from calculations, beginning with NA $= 0.3$, a further increase in NA up to 0.4, 0.5, etc. leads to a noticeable increase in the fifth- and seventh-order coma, which is not compensated by the surface aspherization in the field of view of more than 10 μm, and the resolution decreases. Thus, the optimal numerical aperture of the objective was chosen to be NA $= 0.3$.

For biological applications, the 3D structure of samples is to be determined. In SXRM based on FZPs, for which small numerical apertures and long-focus objectives are typical, this problem is solved using angular tomography, when the sample image is recorded on a detector for each angle of the sample (projection I). Three-dimensional images are reconstructed from such a set of projections with the help of efficient available algorithms and software packages. However, there are a number of restricting factors, in particular, the angular range in which the projections can be obtained; the number of projections; and displacements related to the deviation of the rotation axis from the sample center, which restrict the resolution of the 3D structure by values of 70–100 nm for the lateral resolution of the SXRM restricted by the width of 40–50 nm of the last zone of FZPs used [116, 124].

Because the DOF in SXRMs with a wide-aperture Schwarzschild objective is about 40 nm, the 3D structure of samples in these microscopes can be reconstructed using a considerably simpler z-tomography recording projections corresponding to the displacement of the sample along the optical axis of the microscope. Tomography of this type was not used earlier in the X-ray range, and therefore the development of the corresponding algorithm was required.

We used the algorithm and software developed for z-tomography in visible range microscopy [108]. The specificity of our problem is the presence of strong absorption. In [125], a mathematical model was developed, and all the aspects related to the z-tomography of samples in wide-aperture SXRMs were analyzed.

Figure 14 illustrates the capabilities of the developed method for the reconstruction of the structure of a model cell. Figure 14a shows the specified distribution of the absorption coefficient in a model cell, and Fig. 14b presents the distribution reconstructed from the z-tomography data using the developed model. The reconstruction takes into account the absorption, slope of beams incident on each point of the sample, and the point scattering function (PSF) of the objective. The reconstructed distribution shows substructures related to the PSF. When the PSF is approximated by the delta-function, the reconstructed and model absorption distributions perfectly coincide.

The inset in the lower left part of Fig. 14b shows an enlarged part of the region demonstrating good resolution of structures 40 nm in diameter with the contrast exceeding 50%. Thus, the optical scheme of the SXRM based on a wide-aperture SO and the model for reconstructing the 3D structure of strongly absorbing samples provide a resolution better than 40 nm. At present, the construction of the microscope is being completed and its adjustment has started.

5.4 Maskless X-ray lithography

Modern photolithographs provide a productivity of up to 200 semiconductor plates 300 mm in diameter per hour. Despite the relatively large wavelength of 193 nm, using immersion (193i), a spatial resolution of 42–32 nm was achieved in a simple lithographic process (illumination and the development of a photoresist) and down to 8 nm by using multipatterning technology [126, 127]. The cost of this complexity is the necessity of using many costly masks and

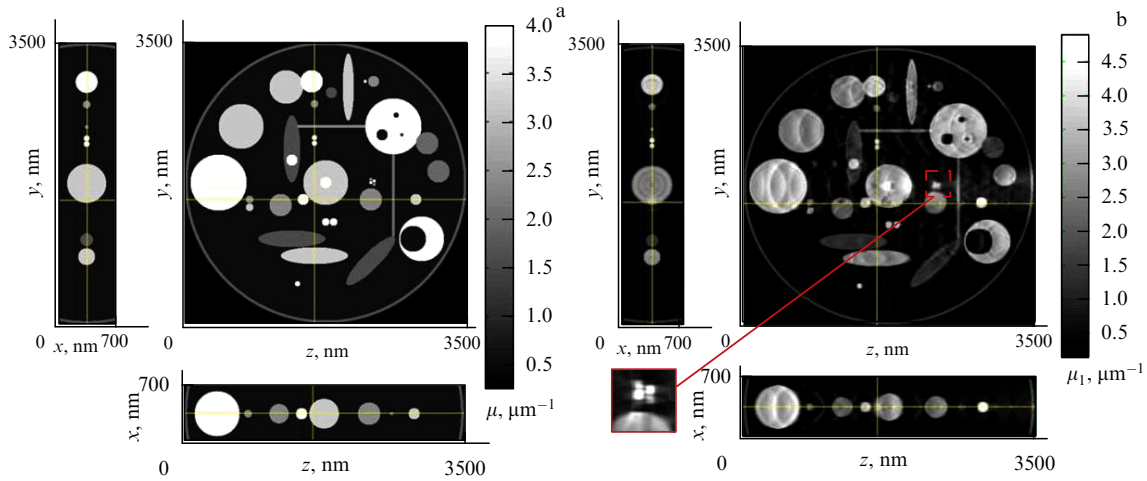

Figure 14. Distributions of the absorption coefficient of a model cell (a) specified in modelling and (b) reconstructed from z-tomography data.

performing additional operations increasing the production cost.

The number of masks and technological operations drastically decreases on moving to a lower wavelength, 13.5 nm, in so-called Extreme Ultraviolet Lithography (EUVL). It was shown in [128] that, beginning with a resolution of 32 nm, the cost of the EUVL process becomes lower than in the 193i technology. However, so far EUVL has not received wide applications because of problems with the productivity ($\approx$ 125 plates per hour), the reliability of the radiation source, and the protection of masks from contaminations [129, 130]. Nevertheless, the continued huge investments in EUVL from leading microcircuit manufacturers such as Intel, Samsung, TSMC (Taiwan Semiconductor Manufacturing Company), and the world's leader ASML (Netherlands) in lithography equipment manufacturing convincingly indicate that EUVL is the next-generation lithography [131, 132].

It is assumed that EUVL technology will provide in the near future a spatial resolution in microcircuits at a level of 2–3 nm. At present, a last-generation scanner provides a spatial resolution of 13 nm for single illumination and 9 nm for double illumination. Therefore, to achieve a resolution of 2–3 nm, it is necessary to solve a number of problems, the main ones being the search for a shorter wavelength [133] and, of course, diffraction-quality multilayer imaging optics. The problems manufacturing these optical elements are similar for X-ray microscopy and X-ray astronomy.

In Russia, EUVL studies are conducted proactively and are mainly concentrated on investigations of individual aspects of this technology [134–138].

The operation of projection lithography requires the existence of a developed infrastructure, including equipment, methods, and technology. One of the most complicated and costly elements of the infrastructure is a diffraction-quality objective and multilayer masks. A set of masks only for manufacturing one chip can cost up to a few million dollars. For this reason, because of the costly equipment and masks and the complicated and costly infrastructure, projection EUVL becomes competitive only in mass production. In other words, EUVL technology requires a global market. All this together makes EUVL technology available only to individual global players (Intel, Samsung, TSMC, Global Foundries).

As a result, EUVL technology is not flexible, which forces the manufacturers of electronic equipment to use commercial microelectronic products in their instruments, even to the detriment of the performance characteristics of their production.

It is known from practice that markets of small- and mid-serial production and mass production are approximately the same as far as cost is concerned. Therefore, the search for new instruments for nanolithography is extremely urgent. A hypothetical 'maskless' nanolithograph should provide a line topological standards provided by projection lithography beginning with 100 nm down to no less than 10 nm. The productivity of such a nanolithograph can be 1–3 orders of magnitude lower than in projection lithography. The cost of the lithographic process should not strongly depend on the production scale. It is also fundamentally important that the lithograph cost be comparable to that of the industrial one-beam electron lithograph. In this case, we can say that nanoelectronics production will be accessible not only to individual global companies but also to small companies.

'Maskless' lithographic methods include electron-beam, ion-beam, and optical lithography and various probe methods of surface modification. All these methods are combined by the programmable formation of topology on a substrate, which can be corrected at any moment by a simple change in scanning algorithms by electron/light beams, a probe, etc. (see, e.g., [139, 140]).

The most universal and developed method is electron-beam lithography, which satisfies almost all requirements on the hypothetical lithograph mentioned above, except the productivity decreasing by 6–7 orders of magnitude with changing topology from the micrometer to nanometer level [139]. The most promising one is assumed to be multi-beam electron lithography. In principle, this technology can provide a fundamental restriction of the resolution at a level of 1 nm. The main problem with electron-beam lithography is related to the interactions of electron beams, which cause image blurring. Although multi-beam electron lithography has already been studied for several dozen years, this problem has not been solved so far. In particular, the best results were obtained by Mapper Technology. The last-generation setup operates with 65 thousand beams and supports technological norms at a level of 28 nm. The elementary beam size is 25 nm, and productivity is up to four plates per hour [141, 142].

However, the 'freezing' of this issue suggests indirectly that the authors encountered difficulties preventing the decrease in topological norms.

Researchers at IPM, RAS are developing an alternative to multi-beam electron lithography — 'maskless' X-ray lithography (MLXRL), first proposed in [143] at a wavelength of 13.5 nm. In MLXRL, the function of a photo mask is executed by a chip with micromirrors controlled by electric signals (Digital Micromirror Device (DMD)). In fact, this technology is a complete analog of multi-beam optical lithography [144], in which the refraction optical elements are replaced by reflection optics. As in optical lithography, a dynamic mask is stationary and a plate with a resist is scanned along two coordinates. Because of the smaller wavelength, the diffraction-limited resolution is automatically transferred to the nanometer region. Although this is clearly a breakthrough technology, the number of publications in this field is small, and they are mainly theoretical [146–149]. The main problem preventing the realization of this idea in practice is related to the absence of DMDs reflecting X-rays.

The situation changed after the publication of paper [150] where the deposition of a multilayer Mo/Si mirror on a DMD with the reflection coefficient of 40% was demonstrated (67%, upon deposition on supersmooth silicon witnesses (plates)). This result demonstrates the fundamental possibility of creating the key element of a maskless X-ray lithograph — a dynamic mask.

At present, a project is being laid out for the development of DMD-based maskless X-ray lithography as part of the complex program of the Ministry of Industry and Trade of the Russian Federation, The Development of the Electronic Industry in the Russian Federation in 2018–2027.

The project is urgent due to the challenges faced by our country, in particular, the necessity to rapidly solve the problem of developing the native technological base for the production of integrated circuits according to the technological norms 65-32/28-22-16/14 nm with the prospect of 7 nm. From the scientific point of view, this is the development of innovative solutions in the field of nanolithography satisfying the modern trends of equipment availability, low operation costs, and the weak dependence of the lithography process cost on the production scale.

Experiments were performed with a DLP9000XBFLS DMD (Texas Instruments) with a period of 7.56 μm and 2560×1600 micromirrors [151]. At the first stage of studies, experiments were performed at the operational wavelength of 13.5 nm. This is explained by the fact that the DMD pixel size is almost 8 μm; therefore, to achieve the nanometer resolution, a diffraction-quality objective reducing the object image up to 10^3 times is required. This results in a low entrance aperture of a projection objective leading to a relatively small part of the radiation used from the radiation source. For practical applications, it is necessary to increase both the X-ray source efficiency and the reflection coefficients of multilayer mirrors. It was shown in [145] that the efficiency of using radiation from a source is inversely proportional to its size. Typical sizes of X-ray laser-plasma sources are 100–200 μm. In [152], a record-breaking small size (about 20 μm) tin ion radiation source emitting at a wavelength of 13.5 nm was reported. The target material of the source is melted tin rotating at a high speed. The tin rotation ensures also a weak contamination of the optical elements produced by the source. This approach can also later be used to develop a radiation source with emission at shorter wavelengths.

Another factor in the choice of the 13.5-nm wavelength is the record-breaking reflection coefficient, about 72%, achieved with the help of multilayer Mo/Be/Si mirrors [138]. However, the further search for shorter wavelengths has not ceased. This concerns both radiation sources and new compositions of multilayer mirrors [153–156].

The productivity of the lithographic process for an experimental lithograph is expected to be about 200 $cm^2\ h^{-1}$, which is already sufficient for small- and mid-sized mass production.

In concluding this section, we consider the fundamentally new method of maskless X-ray lithography proposed in Ref. [157]. A dynamic mask used in this method is a chip of microfocus X-ray tubes. The idea is based on the use of the modern technology of pointed autoemission silicon nanocathodes with a control grid [158] and a thin film target located at a distance of a few micrometers from the control grid. A voltage of $\approx 0.5-3$ kV positive with respect to the cathode is applied to the target. A negative blocking voltage preventing autoemission is simultaneously applied to control the electrodes. When the blocking voltage is removed, an electron microbeam appears, bombarding the target in which the X-ray voltage is generated. Because the target is thin, the absorption depth in the SXR range will be a few tens or hundred nanometers, and if the target is located very close to the cathode, the size of the microbeam on the target and, correspondingly, the X-ray pixel size can also be a few tens or hundred nanometers. Thus, we have an array SX-ray source with computer-controlled pixels.

Since in this scheme the functions of dynamic mask and SX-ray source are combined in one device, the nanolitographic setup is drastically simplified. The chip, the two-mirror objective, and the plate with the resist on a two-dimensional scanner remain [159]. For practical realization, combining and autofocusing systems are also required. Estimates show that, for the average autoemission current density of 1 A cm^{-2}, which was already obtained experimentally in [158], 1 kV applied to a 100-nm-thick beryllium film target and an electron-beam-11.4-nm characteristic $Be_{K\alpha}$ line conversion efficiency $CE \approx 10^{-4}$ [160], the illumination productivity can be expected at levels of 10–20 $cm^2\ h^{-1}$. This simple method is of great interest to researchers and manufacturers of microelectronic chips in small production batches.

The main reserve for increasing the productivity is the decrease in the radiation microbeam size (pixel). Also, the chip size can be increased and thereby so can the electron beam power.

An extremely important problem in projection EUVL is the further decrease in the wavelength. As mentioned, e.g., in Ref. [161], the peak and integrated reflection coefficients of mirrors decrease with decreasing wavelength, and the conversion efficiency of laser-plasma radiation sources decreases, for example, from 5% at a wavelength of 13.5 nm to 1.2–1.5% at a wavelength of 6.7 nm [162]. In the case of X-ray tubes, the conversion efficiency, on the contrary, increases with increasing wavelength. For example, as shown in [159], the lasing efficiency at a wavelength of 3.16 nm of the $N_{K\alpha}$ line is more than an order of magnitude higher than that for the $Be_{K\alpha}$ line, while the calculated lithograph efficiency, taking into account the reflection coefficients of mirrors achieved at present, is more than three times higher. In other words, both the productivity and spatial resolution can be increased in the future.

Thus, maskless lithography provides the high productivity sufficient for practical applications, a high resolution, and flexible technology. Due to a considerable simplification of the X-ray source and all the infrastructure required for its operation in a lithograph, the decrease in the number of mirrors in the scheme, the dimensions, and the energy supply, the technology becomes an order of magnitude cheaper than projection lithography. The removing of masks drastically reduces the cost of the lithographic process and its dependence on the production scale. This nanolithography technology becomes accessible not only to global players but also to smaller research companies. In our opinion, the MLXRL is perfectly suitable to the conditions of the Russian economy (limited access to the world's market, the concentration of industry on unique products, first of all for the military-industrial complex, and supercomputers). And Russian researchers are leaders in this area, which is important.

6. Conclusions

For the last 10–12 years, researchers at IPM, RAS have been creating under laboratory conditions almost from the very beginning advanced production technologies and metrology methods for high-precision and supersmooth optical elements. The technology of shaping high-precision and supersmooth optical elements is based on ion-beam etching. The metrology of the surface shape and roughness is based on methods which can be considered ab initio, which is important, because no method using references, except for specially developed ones and those based on ab initio principles, can ensure the absolute accuracy of measurements. All these developments were used in practice and their efficiency for solving various problems, including some traditional optical applications, was confirmed. The use of such methods considerably broadens the class of realized optical systems and considerably simplifies the fabrication of precise aspherical surfaces, including high-order surfaces (up to 10 or more orders). Measurement methods without references can be used to fabricate and test shape and roughness references for a variety of applications with guaranteed accuracy.

Acknowledgments

The work was performed within the framework of the State Assignment of the IPM, RAS (no. 0035-2014-024) and supported by the Russian Foundation for Basic Research (grant nos 19-07-00173, 19-02-00081, 18-02-173, 18-02-00588, 18-42-520007, 18-32-00671, 18-32-00173).

References

1. Kirz J, Jacobsen, Howells M *Q. Rev. Biophys.* **28** 33 (1995)
2. Wu B, Kumar A *Appl. Phys. Rev.* **1** 011104 (2014)
3. Golub L et al. *Nature* **344** 842 (1990)
4. Gorbunov G G et al. *J. Opt. Technol.* **76** 651 (2009); *Opt. Zh.* **76** (10) 75 (2009)
5. Akopov A K et al. *Kosmonavtika Raketostroenie* (5) 77 (2014)
6. Hoffman, Giallorenzi T G, Slater L B *Appl. Opt.* **54** F268 (2015)
7. Erko A et al. (Eds) *Modern Developments in X-Ray and Neutron Optics* (Berlin: Springer, 2008) p. 533
8. Berglund M et al. *J. Microsc.* **197** 268 (2000)
9. Legall H et al. *Opt. Express* **20** 18362 (2012)
10. Wachulak P W et al. *Opt. Express* **19** 9541 (2011)
11. Takman P A C et al. *J. Microsc.* **226** 175 (2007)
12. Bertilson M et al. *Opt. Express* **17** 11057 (2009)
13. Rehbein S et al. *Phys. Rev. Lett.* **103** 110801 (2009)
14. Vinogradov A V et al. *Zerkal'naya Rentgenovskaya Optika* (Mirror X-ray Optics) (Leningrad: Mashinostroeine, 1989)
15. Platonov Y et al. *Proc. SPIE* **8076** 80760N (2011)
16. Akhsakhalyan A D et al. *Poverkhnost* (1) 5 (2017)
17. Huang Q et al. *Appl. Phys. Rev.* **4** 011104 (2017)
18. Attwood D, Sakdinawat B A *X-Rays and Extreme Ultraviolet Radiation* (Cambridge: Cambridge Univ. Press, 2017)
19. Williamson D M, Zernike E F, Attwood D T *OSA Proc. Extreme Ultraviolet Lithography* **23** 68 (1995)
20. Dinger U et al. *Proc. SPIE* **4146** 35 (2000)
21. Oshino T et al. *Proc. SPIE* **5037** 75 (2003)
22. Chkhalo N I et al. *Appl. Opt.* **55** 619 (2016)
23. Voznesensky N, Zhevlakov A *Proc. SPIE* **5482** 136 (2004)
24. Tan J et al. *Opt. Lett.* **39** 6699 (2014)
25. Malacara D *Optical Shop Testing* (New York: John Wiley and Sons, 1992)
26. Zygo Corporation, http://www.zygo.com
27. Linnik V P *Bull. Acad. Sci. USSR* **1** 208 (1933); *Izv. Akad. Nauk SSSR* **1** 210 (1933)
28. Goldberg K A et al. *J. Vac. Sci. Technol.* **20** 2834 (2002)
29. Sommargren G E *Laser Focus World* **8** 61 (1996)
30. Naulleau P P et al. *Appl. Opt.* **38** 7252 (1999)
31. Otaki K et al. *J. Vac. Sci. Technol. B* **20** 2449 (2002)
32. Voznesensky N B et al. *Tech. Phys.* **52** 271 (2007); *Zh. Tekh. Fiz.* **77** (2) 126 (2007)
33. Zheng M et al. *Chinese Opt. Lett.* **15** 101203 (2017)
34. Salashchenko N N, Toropov M N, Chkhalo N I *Poverkhnost* (7) 3 (2008)
35. Chkhalo N I et al. *Proc. SPIE* **7025** 702507 (2008)
36. Salashchenko N N, Toropov M N, Chkhalo N I *Bull. Russ. Acad. Sci. Phys.* **74** 53 (2010); *Izv. Ross. Akad. Nauk Ser. Fiz.* **74** 62 (2010)
37. Chkhalo N I et al. *Rev. Sci. Instrum.* **79** 033107 (2008)
38. Chkhalo N I et al., in *Lithography* (Ed. M Wang) (London: INTECH, 2010) p. 71
39. Barysheva M M et al. *Phys. Usp.* **55** 681 (2012); *Usp. Fiz. Nauk* **182** 727 (2012)
40. Blunt R, in *Proc. of the CEMANTECH Conf., Vancouver, Canada, April 24 – 27, 2006*, p. 59
41. Griffith J E, Grigg D A *J. Appl. Phys.* **74** R83 (1993)
42. Azarova V V et al. *J. Opt. Technol.* **69** 125 (2002); *Opt. Zh.* **69** (2) 71 (2002)
43. Martínez-Galarce D et al. *Opt. Eng.* **52** 095102 (2013)
44. Barysheva M M et al. *Bull. Russ. Acad. Sci. Phys.* **75** 67 (2011); *Izv. Ross. Akad. Nauk Ser. Fiz.* **75** 71 (2011)
45. Chkhalo N I et al. *Opt. Express* **22** 20094 (2014)
46. Barysheva M M et al. *Proc. SPIE* **8076** 80760M (2011)
47. Barysheva M M et al., in *Fundamentals of Picoscience* (Ed. K D Sattler) (Boca Raton, Fl.: CRC Press. Taylor and Francis Group, 2013) p. 595
48. Holý V, Baumbach T *Phys. Rev. B* **49** 10668 (1994)
49. Kozhevnikov I V, Pyatakhin M V *J. X-Ray Sci. Technol.* **8** 253 (2000)
50. Asadchikov V E et al. *Nucl. Instrum. Meth. Phys. Res. A* **530** 575 (2004)
51. Chkhalo N I, Salashchenko N N, Zorina M V *Rev. Sci. Instrum.* **86** 016102 (2015)
52. Barysheva M M, in *Nanofizika i Nanoelektronika. Trudy XV Mezhdunarodnogo Simpoziuma, 14–18 Marta 2011, Nizhny Novgorod* (Nanophysics and Nanoelectronics. Proc. of the XV Intern. Symp., 14–18 2011, Nizhny Novgorod) Vol. 1 (Nizhny Novgorod: Inst. Fiziki Mikrostruktur RAN, 2011) p. 85
53. Svechnikov M V et al. *Opt. Lett.* **40** 159 (2015)
54. Mahajan V N, Dai G M *J. Opt. Soc. Am. A* **24** 2994 (2007)
55. Svechnikov M V et al. *Opt. Express* **23** 14677 (2015)
56. Karger A M *Appl. Opt.* **12** 451 (1973)
57. Eisenberg N P, Carouby R, Broder J *Proc. SPIE* **1038** 279 (1988)
58. Eklund E R et al. *Phys. Rev. Lett.* **67** 1759 (1991)
59. Ellison J F et al. *Proc. SPIE* **8860** 88600O (2013)
60. Liao W et al. *Opt. Express* **22** 377 (2014)
61. Inaba T et al. *Microelectron. Eng.* **86** 497 (2009)
62. Makeev M A, Cuerno R, Barabasi A-L *Nucl. Instrum. Meth. Phys. Res. B* **197** 185 (2002)
63. Chkhalo N I et al. *Nucl. Instrum. Meth. Phys. Res. A* **603** 62 (2009)

64. Barysheva M M et al. *Bull. Russ. Acad. Sci. Phys.* **76** 163 (2012); *Izv. Ross. Akad. Nauk Ser. Fiz.* **76** 190 (2012)
65. Chkhalo N I et al. *Appl. Opt.* **55** 1249 (2016)
66. Chkhalo N I et al. *Proc. SPIE* **8076** 80760P (2011)
67. Ziegler E et al. *Nucl. Instrum. Meth. Phys. Res. A* **616** 188 (2010)
68. Chen S et al. *Appl. Opt.* **54** 1478 (2015)
69. Chkhalo N I et al. *Appl. Opt.* **57** 6911 (2018)
70. Sidorov D S et al. *Nucl. Instrum. Meth. Phys. Res. B* **387** 73 (2016)
71. Chkhalo N I *Surf. Coat. Tech.* **311** 351 (2017)
72. Chkhalo N I et al. *Appl. Opt.* **58** 3652 (2019)
73. Chkhalo N I et al. *Proc. SPIE* **10235** 102350M (2017)
74. Endo H et al. *Microelectron. Eng.* **87** 982 (2010)
75. Cherezova L A, Mikhailov A V, Zhevlakov A P *J. Opt. Technol.* **73** 812 (2006); *Opt. Zh.* **73** (11) 86 (2006)
76. Xu M et al. *Appl. Opt.* **54** 8055 (2015)
77. Weiser M *Nucl. Instrum. Meth. Phys. Res. B* **267** 1390 (2009)
78. Chkhalo N I et al. *Precision Eng.* **48** 338 (2017)
79. Zhitnik I A et al.. *Tr. Fiz. Inst. Akad. Nauk SSSR* **195** 19 (1989)
80. Sobelman I I et al. *Astron. Lett.* **22** 539 (1996); *Pis'ma Astron. Zh.* **22** 604 (1996)
81. Oraevsky V N, Sobelman I I *Astron. Lett.* **28** 401 (2002); *Pis'ma Astron. Zh.* **28** 457 (2002)
82. Kuzin S V et al. *Solar Syst. Res.* **45** 162 (2011); *Astron. Vestn.* **45** 166 (2011)
83. Andreev S S et al. *Poverkhnost* (1) 6 (2003)
84. Kuzin S V et al. *Bull. Russ. Acad. Sci. Phys.* **75** 87 (2011); *Izv. Ross. Akad. Nauk Ser. Fiz.* **75** 91 (2011)
85. Malyshev I V *Proc. SPIE* **10235** 102350C (2017)
86. Wilson R N *Reflecting Telescope Optics. I Basic Design Theory and its Historical Development* (Rohrbach: Springer Science and Business Media, 2013) p. 43
87. Ponomarev D N *Astronomicheskie Observatorii Sovetskogo Soyuza* (Astronomical Observatories in the Soviet Union) (Moscow: Nauka, 1987)
88. Lew A et al., NASA Technical Report NASA-TM-103443 (1990)
89. Wilson R N, Delabore B *Astron. Astrophys.* **294** 322 (1995)
90. Brooks P *Acta Astronautica* **52** 905 (2003)
91. Middleton E M et al. *IEEE J. Sel. Top. Appl. Earth. Obs. Remote. Sens.* **6** 243 (2013)
92. Korsch D *Appl. Opt.* **13** 2005 (1974)
93. Thales SESO. Space Optics, http://seso.com/new-services/space-optics/
94. Baker J G *Proc. Am. Phil. Soc.* **82** 339 (1940)
95. Schmidt B *Central Zeitung Opt. Mech.* **52** 25 (1931)
96. Brychikhin M N et al. *Appl. Opt.* **55** 4430 (2016)
97. Chkhalo N I et al. *J. Astron. Telescopes Instrum. Syst.* **4** 014003 (2018)
98. Grigoriev I S, Meilikhov E Z (Eds) *Handbook of Physical Quantities* (Boca Raton, Fl.: CRC Press, 1997); Translated from Russian: *Fizicheskie Velichiny. Spravochnik* (Moscow: Energoatomizdat, 1991)
99. Barnes W P *Appl. Opt.* **5** 1883 (1966)
100. Fanson J L et al. *Proc. SPIE* **3356** 478 (1998)
101. Gildner D A, Marder J M *Proc. SPIE* **1485** 46 (1991)
102. Sizenev V S et al. *Voprosy Atom. Nauki Tekh. Ser. Fiz. Rad. Povrezhd. Rad. Materialoved.* (1) 21 (2010)
103. Hashiguchi D, Marder J, Paquin R *Adv. Mater. Process.* **173** 20 (2015)
104. Berglund M et al. *J. Microscopy* **197** 268 (2000)
105. Hanssen E. et al. *J. Struct. Biol.* **177** 224 (2012)
106. Ayele M G et al. *Acta Phys. Polon. A* **129** 237 (2016)
107. Wachulak P W et al. *J. Phys. Conf. Ser.* **849** 012050 (2017)
108. Sage D et al. *Methods* **115** 28 (2017)
109. http://www.nanotech-now.com/news.cgi?story_id = 42612
110. Baghaie A et al. *PLoS One* **12** e0175078 (2017)
111. Tafti A P et al. *Micron* **78** 54 (2015)
112. Khalisov M M "Primenenie atomno-silovoi mikroskopii dlya detektirovaniya otklika nativnykh kletok na vneshnie vozdeisviya" ("Application of atomic force microscopy for detecting the response of native cells to external actions"), Candidate Dissertation (Phys. Tech. Sci.) (St. Petersburg: Institute for Analytical Instrumentation RAS, 2017)
113. Dehlinger A et al. *Proc. SPIE* **9589** 95890 (2015)
114. Kim K W et al. *Phys. Med. Biol.* **51** N99 (2006)
115. Chao W et al. *Opt. Express* **20** 9777 (2012)
116. Weib D et al. *Ultramicroscopy* **84** 185 (2000)
117. Artyukov I A et al. *Quantum Electron.* **25** 919 (1995); *Kvantovaya Elektron.* **22** 951 (1995)
118. Artyukov I A *JETP* **109** 872 (2009); *Zh. Eksp. Teor. Fiz.* **136** 1009 (2009)
119. Ejima T et al. *Opt. Express* **18** 7203 (2010)
120. Panessa-Warren B J, in *X-Ray Microscopy. Proc. of the Intern. Symp., Gottingen, Fed. Rep. of Germany, September 14 – 16, 1983* (Eds G Schmahl, D Rudolph) (Berlin: Springer-Verlag, 1984) p. 268; Translated into Russian: *Rentgenovskaya Optika i Mikroskopiya* (Moscow: Mir, 1987) p. 359
121. Chkhalo N I et al. *Rev. Sci. Instrum.* **86** 063701 (2015)
122. Malyshev I V *Poverkhnost* (1) 3 (2019)
123. Andreev S S et al. *J. Synchrotron Radiat.* **10** 358 (2003)
124. Bertilson M *Opt. Lett.* **36** 2728 (2011)
125. Malyshev I V et al. *Ultramicroscopy* **202** 76 (2019)
126. Kim K et al. *Proc. SPIE* **8326** 832605 (2012)
127. Scotten Jones (2018), https://seekingalpha.com/article/4151376-tsmc-intel-lead-semiconductor-processes
128. Wood O et al. *Proc. SPIE* **8322** 832203 (2012)
129. Neisser M, Wurm S *Adv. Opt. Technol.* **4** 235 (2015)
130. Turkot B, Phillips M, in *Proc. of the Intern. Workshop on EUV and Soft X-Ray Sources, Dublin, 2015*, p. 1; http://www.euvlitho.com/2015/S1.pdf
131. Kim S S et al. *Proc. SPIE* **10143** 1014306 (2017)
132. Levinson H J, in *Proc. of the Intern. Workshop on EUV Lithography, June 13–16, Berkeley CA, 2016*, p. 1; http://www.euvlitho.com/2016/P1.pdf
133. Wagner C, Harned N *Nature Photon.* **4** 24 (2010)
134. Koshelev K N, Banine V E, Salashchenko N N *Phys. Usp.* **50** 741 (2007); *Usp. Fiz. Nauk* **177** 777 (2007)
135. Salashchenko N N, Chkhalo N I *Herald Russ. Acad. Sci.* **78** 279 (2008); *Vestn. Ross. Akad. Nauk* **78** 450 (2008)
136. Chkhalo N I et al. *J. Micro/Nanolith. MEMS MOEMS* **11** 021123 (2012)
137. Chkhalo N I et al. *J. Micro/Nanolith. MEMS MOEMS* **11** 021115 (2012)
138. Chkhalo N I et al. *Opt. Lett.* **42** 5070 (2017)
139. Menon R et al. *Mater. Today* **8** (2) 26 (2005)
140. Belokopytov G V, Ryzhikova Yu V *Mikroelektronika* **40** 453 (2011)
141. Mapper Lithography, https://mapper.nl/
142. Servin I et al. *Proc. SPIE* **9423** 94231C (2015)
143. Choksi N et al. *J. Vac. Sci. Technol. B* **17** 3047 (1999)
144. Menon R, Patel A, Smith H I *Proc. SPIE* **5721** 53 (2005)
145. Chkhalo N I et al. *Proc. SPIE* **10224** 102241O1 (2016)
146. Shroff Y A, Chen Y, Oldham W G *Proc. SPIE* **5374** 637 (2004)
147. Chen Y, Shroff Y *Proc. SPIE* **6151** 61512D (2006)
148. Chen Y *Proc. SPIE* **8323** 83231Q (2012)
149. Johnson K C *J. Vac. Sci. Technol. B* **30** 051606 (2012)
150. Chkhalo N et al. *J. Vac. Sci. Technol. B* **35** 062002 (2017)
151. Texas Instruments, http://www.ti.com/lit/ds/symlink/dlp9000x.pdf
152. Vinokhodov A Yu et al., in *Nanofizika i Nanoelektronika. Trudy XXIII Mezhdunarodnogo Simpoziuma, 11–14 Marta 2019 g., Nizhny Novgorod* (Nanophysics and Nanoelectronics. Proc. of the XXIII Intern. Symp., 11–14 March 2019, Nizhny Novgorod) Vol. 1 (Nizhny Novgorod: Izd. Nizhegorod. Gos. Univ. im. N.I. Lobachevskogo, 2019) p. 436
153. Chkhalo N I et al. *AIP Adv.* **8** 105003 (2018)
154. Svechnikov M V et al. *Opt. Express* **26** 33718 (2018)
155. Shalashov A G et al. *Appl. Phys. Lett.* **113** 153502 (2018)
156. Belik V P et al. *Tech. Phys. Lett.* **43** 1001 (2017); *Pis'ma Zh. Tekh. Fiz.* **43** (22) 10 (2017)
157. Salashchenko N N, Chkhalo N I, Dyuzhev N A *Poverkhnost* (10) 10 (2018)
158. Basu A et al. *J. Phys. D* **48** 225501 (2015)
159. Chkhalo N I et al. *Proc. SPIE* **11022** 110221M (2019)
160. Lopatin A Ya et al. *JETP* **127** 985 (2018); *Zh. Eksp. Teor. Fiz.* **154** 1067 (2018)
161. Chkhalo N I, Salashchenko N N *AIP Adv.* **3** 082130 (2013)
162. Otsuka T et al. *Proc. SPIE* **8322** 832214 (2012)